Atmos. Meas. Tech., 10, 3041–3055, 2017
https://doi.org/10.5194/amt-10-3041-2017

Atmospheric Measurement Techniques
Open Access

A statistical comparison of cirrus particle size distributions measured using the 2-D stereo probe during the TC^4, SPARTICUS, and MACPEX flight campaigns with historical cirrus datasets

M. Christian Schwartz

Environmental Science Division, Argonne National Laboratory, 9700 Cass Avenue, Bldg. 240, 6.A.15, Lemont, IL 60439, USA

Correspondence to: M. Christian Schwartz (mcschwar@umich.edu)

Received: 16 February 2017 – Discussion started: 20 March 2017
Revised: 29 June 2017 – Accepted: 30 June 2017 – Published: 23 August 2017

Abstract. This paper addresses two straightforward questions. First, how similar are the statistics of cirrus particle size distribution (PSD) datasets collected using the Two-Dimensional Stereo (2D-S) probe to cirrus PSD datasets collected using older Particle Measuring Systems (PMS) 2-D Cloud (2DC) and 2-D Precipitation (2DP) probes? Second, how similar are the datasets when shatter-correcting post-processing is applied to the 2DC datasets? To answer these questions, a database of measured and parameterized cirrus PSDs – constructed from measurements taken during the Small Particles in Cirrus (SPARTICUS); Mid-latitude Airborne Cirrus Properties Experiment (MACPEX); and Tropical Composition, Cloud, and Climate Coupling (TC^4) flight campaigns – is used.

Bulk cloud quantities are computed from the 2D-S database in three ways: first, directly from the 2D-S data; second, by applying the 2D-S data to ice PSD parameterizations developed using sets of cirrus measurements collected using the older PMS probes; and third, by applying the 2D-S data to a similar parameterization developed using the 2D-S data themselves. This is done so that measurements of the same cloud volumes by parameterized versions of the 2DC and 2D-S can be compared with one another. It is thereby seen – given the same cloud field and given the same assumptions concerning ice crystal cross-sectional area, density, and radar cross section – that the parameterized 2D-S and the parameterized 2DC predict similar distributions of inferred shortwave extinction coefficient, ice water content, and 94 GHz radar reflectivity. However, the parameterization of the 2DC based on uncorrected data predicts a statistically significantly higher number of total ice crystals and a larger ratio of small ice crystals to large ice crystals than does the parameterized 2D-S. The 2DC parameterization based on shatter-corrected data also predicts statistically different numbers of ice crystals than does the parameterized 2D-S, but the comparison between the two is nevertheless more favorable. It is concluded that the older datasets continue to be useful for scientific purposes, with certain caveats, and that continuing field investigations of cirrus with more modern probes is desirable.

1 Introduction

For decades, in situ ice cloud particle measurements have often indicated ubiquitous high concentrations of the smallest ice particles (Korolev et al., 2013a; Korolev and Field, 2015). If the smallest ice particles are indeed always present in such large numbers, then their effects on cloud microphysical and radiative properties are pronounced. For instance, Heymsfield et al. (2002) reported small particles dominating total particle concentrations (N_{T}s) at all times during multiple Tropical Rainfall Measuring Mission (TRMM) field campaigns, while Field (2000) noted the same phenomenon in midlatitude cirrus. Lawson et al. (2006) reported N_{T}s in midlatitude cirrus ranging from $\sim .03$ to $8\,\mathrm{cm}^{-3}$ and estimated that particles smaller than 50 µm were responsible for 99 % of N_{T}, 69 % of shortwave extinction, and 40 % of ice water content (IWC). From several representative cirrus cases, Gayet et al. (2002) reported average N_{T}s as high as $10\,\mathrm{cm}^{-3}$ and estimated that particles having maximum dimensions smaller than 15.8 µm resulted in about 38 % of measured

Published by Copernicus Publications on behalf of the European Geosciences Union.

shortwave extinction, and Gayet et al. (2004, 2006) estimated from a broader set of measurements that particles smaller than 20 µm accounted for about 35 % of observed shortwave extinction. Garrett et al. (2003) estimated that small ice crystals, with equivalent radii less than 30 µm, contributed in excess of 90 % of total shortwave extinction during the NASA Cirrus Regional Study of Tropical Anvils and Cirrus Layers – Florida Area Cirrus Experiment (CRYSTAL-FACE).

While it is quite possible for relatively high numbers of small ice crystals to occur naturally (see, e.g., Zhao et al., 2011; Heymsfield et al., 2017), it is also possible for small-ice-particle concentrations to be significantly inflated by several measurement artifacts. The various particle size distribution (PSD) probes (also known as single-particle detectors) in use employ a handful of different measurement techniques to detect and size particles across a variety of particle size ranges. The units of a PSD are number of particles per unit volume per unit size. Thus, after a PSD probe counts the particles that pass through its sample area, each particle is assigned a size as well as an estimate of the sample volume from which it was drawn (Brenguier et al., 2013). Uncertainty in any of these PSD components results in uncertain PSD estimates.

Leaving aside technologies still under development and test, such as the Holographic Detector of Clouds (HOLODEC; Fugal and Shaw, 2009), PSD probes fall into three basic categories: impactor probes, light-scattering probes, and imaging probes. (More thorough discussions on this topic, along with comprehensive bibliographies, may be found in Brenguier et al. (2013) and in Baumgardner et al. (2017).) The earliest cloud and precipitation particle probes were of the impactor type (Brenguier et al., 2013). Modern examples include the Video Ice Particle Sampler (VIPS; Heymsfield and McFarquhar, 1996), designed to detect particles in the range 5–200 µm. The basic operating principle is thus: cloud and precipitation particles impact upon a substrate, leaving an imprint (or leaving the particle itself) to be replicated (in the case of the VIPS, by digital imaging) and analyzed. This type of probe is particularly useful for imaging the smallest ice crystals (Baumgardner et al., 2011; Brenguier et al., 2013).

Light-scattering probes also are designed for detecting small spherical and quasi-spherical particles (a typical measurement range would be 1–50 µm; see Baumgardner et al., 2017). These work by measuring, at various angles, the scatter of the probe's laser due to the presence of a particle within the probe's sample area. Assuming that detected particles are spherical and assuming their index of refraction, Mie theory is then inverted to estimate particle size. Two prominent examples of this type of probe are the Forward Scattering Spectrometer Probe (FSSP; Knollenberg, 1976, 1981) and the Cloud Droplet Probe (CDP; Lance et al., 2010).

Imaging probes, also known as optical array probes (OAPs), use arrays of photodetectors to make two-dimensional images of particles that pass through their sample areas. Unlike the light-scattering probes, OAPs make no assumptions regarding particle shape or composition (Baumgardner et al., 2017), and they have broader measurement ranges aimed both at cloud and precipitation particles. Two prominent examples are the Two-Dimensional Stereo (2D-S; Lawson et al., 2006) probe, whose measurement range is 10–1280 µm, and the Two-Dimensional Cloud (2DC; Knollenburg, 1976) probe, whose measurement range is 25–800 µm. OAPs designed for precipitation particle imaging include the Precipitation Imaging Probe (PIP; Baumgardner et al., 2001) and the High Volume Precipitation Spectrometer (HVPS; Lawson et al., 1998), which measure particles ranging from ~ 100 µm up to several millimeters.

Because an estimate of the sample volume from which a particle is drawn is a function of the particle's size and assumes that the particle is spherical (Brenguier et al., 2013), all PSD probes suffer from sample volume uncertainty. Estimated sample volumes from OAPs perforce suffer from the problem of sizing aspherical particles from 2-D images (see Figs. 5–40 of Brenguier et al., 2013). Nonetheless, impactor and light-scattering probes both suffer from much smaller sample volumes than do OAPs (Brenguier et al., 2013; Baumgardner et al., 2017; Heymsfield et al., 2017). Scattering probes, for example, need up to several times the sampling distance in cloud as OAPs to produce a statistically significant PSD estimate (see Figs. 3–5 of Brenguier et al., 2013).

The obvious difficulty in sizing small ice crystals with light-scattering probes is the application of Mie theory to nonspherical ice crystals. Probes such as the FSSP and CDP are therefore prone to undersizing ice crystals (Baumgardner et al., 2011, 2017; Brenguier et al., 2013).

Imaging particles using an OAP requires no assumptions regarding particle shape or composition, but sizing algorithms based on two-dimensional images are highly sensitive to particle orientation (Brenguier et al., 2013). Other sizing uncertainties stem from imperfect thresholds for significant occultation of photodiodes, the lack of an effective algorithm for bringing out-of-focus ice particles into focus, and the use of statistical reconstructions of partially imaged ice crystals that graze a probe's sample area (Brenguier et al., 2013; Baumgardner et al., 2017).

Ideally, PSDs estimated using different probes would be stitched together in order to provide a complete picture of the ice particle population, from micron-sized particles through snowflakes (Brenguier et al., 2013). However, while data from VIPS, fast FSSP, and Small Ice Detector-3 (SID-3; Ulanowski et al., 2014) probes are available to complement the OAP data used in this study, none of them are used on account of sizing uncertainties stemming from their small sample volumes and from spherical particle assumptions. The two publications wherewith comparison is made in this paper also restricted their datasets to OAPs.

The substantial remaining source of small particle counting and sizing dealt with in this study is particle shattering.

Shattering of ice particles on probe tips and inlets and on aircraft wings has rendered many historical cirrus datasets suspect (Vidaurre and Hallet, 2009; Korolev et al., 2011; Baumgardner et al., 2017) due to such shattering artificially inflating measurements of small-ice-particle concentrations (see, e.g., McFarquhar et al., 2007; Jensen et al., 2009; Zhao et al., 2011). Measured ice PSDs are used to formulate parameterizations of cloud processes in climate and weather models, so the question of the impact of crystal shattering on the historical record of ice PSD measurements is one of significance (Korolov and Field, 2015).

Post-processing of optical probe data based on measured particle inter-arrival times (Cooper, 1978; Field et al., 2003, 2006; Lawson, 2011; Jackson et al., 2014; Korolev and Field, 2015) has become a tool for ameliorating contamination from shattered artifacts. Shattered-particle removal is based on modeling particle inter-arrival times by a Poisson process, assuming that each inter-arrival time is independent of all other inter-arrival times. Jackson and McFarquhar (2014) posit that particle clustering (Hobbs and Rangno, 1985; Kostinski and Shaw, 2001; Pinsky and Khain, 2003; Khain et al., 2007), which would violate this basic assumption, is not likely a matter of significant concern as cirrus particles are naturally spread further apart than are liquid droplets and sediment over a continuum of size-dependent speeds.

In addition, a posteriori shattered-particle removal should be augmented with design measures such as specialized probe arms and tips (Vidaurre and Hallet, 2009; Korolov et al., 2011, 2013a; Korolev and Field, 2015). Probes must also be placed away from leading wing edges (Vidauure and Hallet, 2009; Jensen et al., 2009), as many small particles generated by shattering on aircraft parts are likely not be filtered out by shatter-recognition algorithms.

The ideal way to study the impact of both shattered-particle removal and improved probe design is to fly two versions of a probe – one with modified design and one without – side by side and then to compare results from both versions of the probe both with and without shattered-particle removal. Results from several flight legs made during three field campaigns where this was done are described in three recent papers: Korolev et al. (2013b), Jackson and McFarquhar (2014), and Jackson et al. (2014). Probes built for several particle size ranges were examined, but those of interest here are the 2D-S and the older 2DC. Three particular results distilled from those papers are useful here.

First, in agreement with Lawson (2011), a posteriori shattered-particle removal is more effective at reducing counts of apparent shattering fragments for the 2D-S than are modified probe tips. The opposite is true for the 2DC. This is attributed to the 2D-S's larger sample volume; to its improvements in resolution and electronic time response over the 2DC; and to its 256 photodiode elements (Jensen et al., 2009; Lawson, 2011; Brenguier et al., 2013), which allow it to size particles smaller than 100 µm and to measure particle inter-arrival times more accurately (Lawson et al., 2010; Korolev et al., 2013b; Brenguier et al., 2013).

Second, shattered artifacts seem mainly to corrupt particle size bins less than about 500 µm (see also Baumgardner et al., 2011). Thus Korolev et al. (2013b) posit that bulk quantities computed from higher-order PSD moments – such as shortwave extinction coefficient, IWC, and radar reflectivity – are likely to compare much better between the 2D-S and the 2DC than is N_{T} (see also Jackson and McFarquhar, 2014; Heymsfield et al., 2017).

Third, the efficacy of shattered-particle removal from the 2DC is questionable: the post-processing is prone to accepting shattered particles and to rejecting real particles (Korolev and Field, 2015). The parameters of the underlying Poisson model and its ability to correctly identify shattered fragments depend on the physics of the cloud being sampled (Vidaurre and Hallett, 2009; Korolev et al., 2011), and the older 2DC experiences more issues with instrument depth of field, unfocused images, and image digitization than do newer OAPs, further compounding uncertainty in the shattered-particle removal (Korolev et al., 2013b; Korolev and Field, 2015).

In the context of relatively small studies such as these, Korolev et al. (2013b) pose two questions: (i) to what extent can the historical data be used for microphysical characterization of ice clouds, and (ii) can the historical data be reanalyzed to filter out the data affected by shattering? One difficulty in addressing these questions is the scarcity of data from side-by-side instrument comparisons. Another is that, especially for the 2DC, "correcting [data] a posteriori is not a satisfactory solution" (Vidaurre and Hallet, 2009). However, shattered-particle removal is the main (if not the only) correction method available when revisiting historical datasets.

In order to address the first question of Korolev et al. (2013b), bulk cloud properties derived from shatter-corrected 2D-S data are used to answer two questions: (1) how similar are the statistics of cirrus PSD datasets collected using the 2D-S probe to cirrus PSD datasets collected using older 2DC and 2DP (2-D Precipitation) probes? (2) How similar are the datasets when shatter-correcting post-processing is applied to the 2DC datasets? In proceeding, two points are critical to recall. First, the 2D-S is reasonably expected to give results superior to the 2DC after shattered-particle removal. Second, lingering uncertainty notwithstanding, results presented elsewhere from the shatter-corrected 2D-S reveal behaviors in ice microphysics within different regions of cloud that are expected both from physical reasoning and from modeling studies and that were not always discernible before from in situ datasets (Lawson, 2011; Schwartz et al., 2014).

To this end, a substantial climatology of shatter-corrected, 2D-S-measured cirrus PSDs is indirectly compared with two large collections of older datasets, collected from the early 1990s through the mid-2000s mainly using Particle Measurement Systems 2DC and 2DP (Baumgardner, 1989) as well as Droplet Measurement Technologies Cloud Imaging Probe

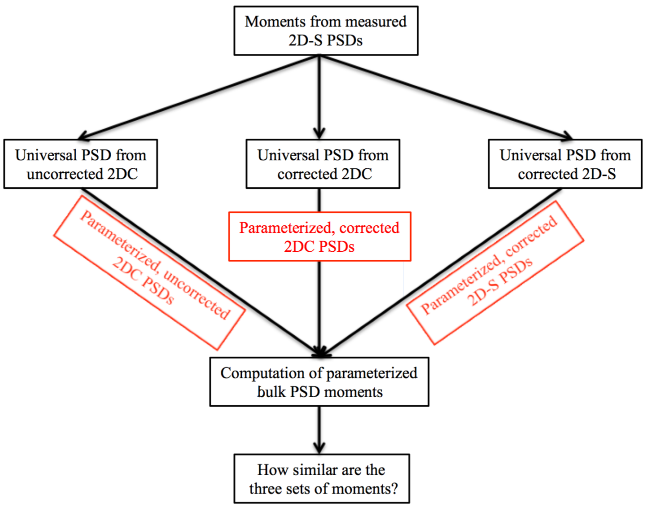

Figure 1. Flowchart illustrating the method of comparison between the parameterized shatter-corrected 2DC–2DP dataset, uncorrected 2DC–2DP dataset, and shatter-corrected 2D-S dataset.

(CIP) and PIP instruments (Heymsfield et al., 2009) and, in one instance, the 2D-S. The older datasets are presented and parameterized in Delanoë et al. (2005; hereinafter D05) and in Delanoë et al. (2014; hereinafter D14). The data used in D05 were not subject to shattered-particle removal, whereas the data in D14 were a posteriori.

The comparison strategy, in short is as follows. The D05 and D14 parameterizations consist of normalized, "universal" cirrus PSDs to which functions of PSD moments are applied as inputs. The results of so doing are sets of parameterized 2DC PSDs – both shatter-corrected and uncorrected. To make the comparison, the same moments from 2D-S-measured PSDs are applied to the D05 and D14 parameterizations in order to simulate what the shatter- and non-shatter-corrected 2DCs would have measured had they flown with the 2D-S. Then, a universal PSD derived from the 2D-S itself is computed in order to make a fair comparison. The moments from the 2D-S-measured PSDs are applied to the 2D-S universal PSD, and it is then seen whether the older datasets differ statistically from the newer in their derived cirrus bulk properties. This procedure is illustrated in Fig. 1.

Section 2 contains a description of the data used herein. Section 3 discusses the fitting of PSDs with gamma distributions for computational use, Sect. 4 discusses the normalization and parameterization schemes used by D05 and D14, and Sect. 5 discusses the effects of not having included precipitation probe data with the 2D-S data. Section 6 demonstrates the final results of the comparison and concludes with a discussion.

2 Data

The 2D-S data were collected during the Mid-Latitude Airborne Cirrus Experiment (MACPEX), based in Houston, TX, during February and March 2011 (MACPEX Science Team, 2011); the Small Particles in Cirrus (SPARTICUS) campaign, based in Oklahoma during January through June 2010 (SPARTICUS Science Team, 2010); and TC^4, based in Costa Rica during July 2007 (TC^4 Science Team, 2007). The SPEC 2D-S probe (Lawson, 2011) images ice crystal cross sections via two orthogonal lasers that illuminate two corresponding linear arrays of 128 photodiodes. PSDs, as well as distributions of cross-sectional area and estimated mass, are reported every second in 128 size bins with centers starting at 10 µm and extending out to 1280 µm. Particles up to about 3 mm can be sized in one dimension by recording the maximum size along the direction of flight. During SPARTICUS the 2D-S flew aboard the SPEC Inc. Learjet, while during MACPEX it was mounted on the NASA WB57 aircraft. During TC^4 it was mounted on both the NASA DC8 and the NASA WB57, but the WB57 data are not used due to documented contamination of the data from shattering artifacts off of the aircraft wing (Jensen et al., 2009).

Temperature was measured during MACPEX, TC^4, and SPARTICUS using a Rosemount total temperature probe. Bulk IWC measurements are available for MACPEX from the Closed-path tunable diode Laser Hygrometer (CLH) probe (Davis et al., 2007). Condensed water that enters the CLH is evaporated so that a measurement of total water can be made. The condensed part of the total water measured by the CLH is obtained by estimating condensed water mass from concurrent PSDs measured by the National Center for Atmospheric Research (NCAR) VIPS probe and then subtracting this estimate from the measured total water mass.

3 Parametric fitting of PSDs

PSDs measured by the 2D-S were fit with both unimodal and bimodal parametric gamma distributions. The unimodal distribution is

$$n(D) = N_0 (D/D_0)^{\alpha} \exp(-D/D_0), \tag{1}$$

where D is particle maximum dimension, D_0 is the scale parameter, α is the shape parameter, and N_0 is the so-called intercept parameter. The bimodal distribution is simply a mixture of two unimodal distributions:

$$n(D) = N_{01}(D/D_{01})^{\alpha_1} \exp(-D/D_{01}) + N_{02}(D/D_{02})^{\alpha_2} \exp(-D/D_{02}). \tag{2}$$

Save in a handful of instances (which will be indicated), all bulk PSD quantities shown here are computed using these parametric fits. A combination of unimodal and bimodal fits is used to compute N_{T}, dictated by the shape of the PSD as

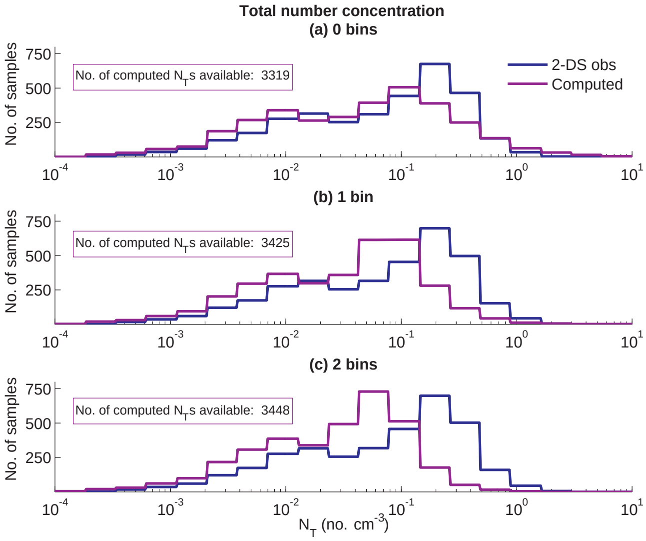

Figure 2. Comparisons of computed and measured total number concentration for 15 s PSD averages and for truncation of none through the first two PSD size bins.

determined by a generalized chi-squared goodness-of-fit test (Schwartz, 2014). Unimodal fits are used to compute all other bulk quantities.

Unimodal fits were performed via the method of moments (in a manner similar to Heymsfield et al., 2002). Both the method of moments and an expectation maximization algorithm (Moon, 1996; Schwartz, 2014) were used for the bimodal fits – the more accurate of those two fits (as determined by whether fit provided the smaller binned Anderson–Darling test statistic; Demortier, 1995) being kept.

Measured PSDs are both truncated and time-averaged in order to mitigate counting uncertainties. It is here assumed that temporal averaging sufficiently reduces Poisson counting noise so that it may be ignored (see, e.g., Gayet et al., 2002). Given already-cited concerns regarding uncertainty in shattered-particle removal, the smallest size bins are not automatically assumed here to be reliable. Other competing uncertainties further complicate particle counts within the first few size bins, e.g., decreased detection efficiency within the first size bin (Baumgardner et al., 2017), the possible underestimation of counts of real particles by a factor of 5–10 (Gurganus and Lawson, 2016), and mis-sizing of larger particles into smaller size bins due to image breakup at the edge of the instrument's depth of field (Korolev et al., 2013b; Korolev and Field, 2015; Baumgardner et al., 2017).

In order to determine how many of the smallest size bins to truncate and for how many seconds to average in order to make the counting assumption valid, two simple exercises were performed using the MACPEX dataset. In the first exercise, 15 s temporal averages were performed along with truncating zero through two of the smallest size bins while only the unimodal fits (chosen according to a maximum-likelihood ratio test; Wilks, 2006) were kept. This exercise was performed first so as to prevent the most spurious size bins interfering with the smoothing out of Poisson counting noise. Figure 2 shows comparisons of distributions of measured and computed (from the fits) N_{T}s. The difference in the number of samples of computed N_{T} between zero bins and one bin truncated is an order of magnitude higher than that between one bin and two bins truncated. This is due to frequent, extraordinarily high numbers of particles recorded in the smallest size bin that at times cause a PSD to be flagged as bimodal by the maximum-likelihood ratio test. As this effect lessens greatly after truncating only one bin, and as the computed and measured N_{T}s are otherwise better matched using a single-bin truncation, the smallest size bin is ignored for all PSDs (making the smallest size bin used 15–25 µm).

Also, IWC was estimated from the fit distributions (the first size bin having been left off in the fits) using the mass–dimensional relationship $m(D) = 0.0065 D^{2.25}$ (m denotes mass, and all units are cgs) given in Heymsfield (2003) for midlatitude cirrus. The distribution of IWC thus computed nominally matches (not shown) IWC estimates from the both CLH and from the 2D-S data product, which uses mass-projected area relationships (Baker and Lawson, 2006).

For the second exercise, temporal averages from 1 to 20 s were performed, truncating the first size bin and again keeping only the unimodal fits. The balance to strike in picking a temporal average length is to smooth out Poisson counting uncertainties acceptably without losing physical information to an overlong average. Qualitatively, the statistics of the fit parameters begin to steady at around 15 s (not shown), so a 15 s temporal average was chosen. Using the data filters, temporal average, and bin truncation thus far described results in $\sim$ 17 000 measured PSDs and their accompanying fits.

It must be noted that the first 2D-S size bin contains at least some real particles, though the aforementioned uncertainties make it impossible (at present) to know how many. Therefore, N_{T}s computed from the remaining bins can be underestimates. Parametric fits extrapolate the binned data all the way to size zero, though; so it could be assumed, if the real ice particle populations are in fact gamma-distributed, that this extrapolation is a fair estimate of the real particles lost due to truncating the first size bin. In truth, however, the assumption of a gamma-shaped PSD is arbitrary, if convenient, but the gamma PSD shape is kept for its convenience and for its ability to reproduce higher-order PSD moments. However, in this paper – where N_{T}s (equivalently, the zeroth moments) from the parametric, the binned, or the normalized parametric PDSs are computed – the computations are begun at the left edge of the second size bin so as to compare equivalent quantities. In other words, N_{T}s presented for comparison here are truncated to compensate for having left off the smallest size bin.

4 Normalization and parameterization

In this section, the functions of 2D-S-measured PSD moments that are applied to the D05 and D14 parameterizations (see Fig. 1) are explained. However, the D05 and D14 parameterizations make use of PSDs in terms of equivalent melted diameter D_{eq}. Before computing any moments, it is therefore necessary first to transform all 2D-S-measured PSDs from functions of maximum dimension D to functions of equivalent melted diameter D_{eq}.

Each 2D-S-measured PSD $n_D(D)$, whose independent variable is ice particle maximum dimension, is transformed to a distribution $n_{D_{\mathrm{eq}}}(D_{\mathrm{eq}})$, whose independent variable is equivalent melted diameter. The transformations are performed twice: once using the density–dimensional relationship used in D05 and once using a mass–dimensional relationship used in D14. The first transformation allows for application of the 2D-S data to the D05 parameterization, and the second first transformation allows for application of the 2D-S data to the D14 parameterization.

The density–dimensional relationship $\rho(D) = aD^b$ (ρ denotes density, D denotes particle maximum dimension, the power law coefficients are $a = 0.0056$ and $b = -1.1$, and all units are cgs) used in D05 stems from relationships published by Locatelli and Hobbs (1974) and Brown and Francis (1995) for aggregate particles. Setting masses equal as in D05 results in the independent variable transformation

$$D_{\mathrm{eq}} = \left(\frac{aD^b}{\rho_{\mathrm{w}}}\right)^{1/3} D, \tag{3}$$

where ρ_{w} is the density of water.

The mass–dimensional relationship labeled “composite” (Heymsfield et al., 2010) in D14 is used here for the second transformation:

$$m(D) = 7e^{-3}D^{2.2} = a_{\mathrm{m}}D^{b_{\mathrm{m}}}.$$

(Here, m denotes mass, the power law coefficients are $a_{\mathrm{m}} = 7e^{-3}$ and $b_{\mathrm{m}} = 2.2$, and all units are cgs.) Setting masses equal results in the independent variable transformation

$$D_{\mathrm{eq}} = \left(\frac{6a_{\mathrm{m}}}{\pi\rho_{\mathrm{w}}}\right)^{1/3} D^{b_{\mathrm{m}}/3}. \tag{4}$$

The “composite” relation was only used to normalize about 54 % of the PSDs utilized in D14; however, those datasets so normalized are broadly similar to MACPEX, SPARTICUS, and TC^4 (one in fact is TC^4, where the Cloud Imaging Probe was used as well as the 2D-S), and so the “composite” relation is used here for comparison with D14.

Following the notation of D05 and D14 notation, transformed PSDs then have their independent variable scaled by mass-mean diameter

$$D_{\mathrm{m}} = \frac{\int_0^\infty D_{\mathrm{eq}}^4 n_{D_{\mathrm{eq}}}(D_{\mathrm{eq}})\,\mathrm{d}D_{\mathrm{eq}}}{\int_0^\infty D_{\mathrm{eq}}^3 n_{D_{\mathrm{eq}}}(D_{\mathrm{eq}})\,\mathrm{d}D_{\mathrm{eq}}} \tag{5}$$

and their ordinates scaled by

$$N_0^* = \frac{4^4}{\Gamma(4)} \frac{\left[\int_0^\infty D_{\mathrm{eq}}^3 n_{D_{\mathrm{eq}}}(D_{\mathrm{eq}})\,\mathrm{d}D_{\mathrm{eq}}\right]^5}{\left[\int_0^\infty D_{\mathrm{eq}}^4 n_{D_{\mathrm{eq}}}(D_{\mathrm{eq}})\,\mathrm{d}D_{\mathrm{eq}}\right]^4}, \tag{6}$$

so that

$$n_{D_{\mathrm{eq}}}(D_{\mathrm{eq}}) = N_0^* F\left(x = \frac{D_{\mathrm{eq}}}{D_{\mathrm{m}}}\right). \tag{7}$$

In Eq. (7), $F(x)$ is, ideally, the universal, normalized PSD (Meakin, 1992; Westbrook et al., 2004a, b; D05; Tinel et al., 2005; D14). The quantities N_0^* and D_{m} are the functions of 2D-S-measured PSD moments that are required for application to the D05/D14 parameterizations in order to produce parameterized, corrected 2DC PSDs and parameterized, uncorrected 2DC PSDs (see Fig. 1). The procedure for transforming and normalizing the 2D-S-measured PSDs and for computing N_0^* and D_{m} will now be explained.

Starting with binned PSDs, the normalization procedure is wended as described in Sect. 4.1 of D05. First, the 2D-S bin centers and bin widths are transformed once using Eq. (3) for the comparison with D05 and once again using Eq. (4) for the comparison with D14. Next, each binned PSD is transformed by scaling from D space to D_e space (see below). Then, via numerically computed moments, Eqs. (5)–(7) are used to produce one N_0^*–D_{m} pair for each measured PSD and to normalize the binned mass-equivalent spherical PSDs, which are then grouped into normalized diameter bins of $\Delta x = 0.10$.

The scale factor for transforming binned PSDs is derived using this simple consideration: if the number of particles within a size bin is conserved upon the bin's transformation from D space to D_{eq} space, then, given that the transformation is from maximum dimension to mass-equivalent spheres, so also is the mass of the particles within a size bin conserved. That is,

$$n_{D_{\mathrm{eq}}}(D_{\mathrm{eq}_i}) = n_D(D_i)\frac{aD_i^{b+3}\Delta D_i}{\rho_{\mathrm{w}}D_{\mathrm{eq}_i}^3\Delta D_{\mathrm{eq}_i}} \tag{8}$$

for the D05 transformation and

$$n_{D_{\mathrm{eq}}}(D_{\mathrm{eq}_i}) = n_D(D_i)\frac{a_{\mathrm{m}}D_i^{b_{\mathrm{m}}}\Delta D_i}{\left(\frac{\pi}{6}\right)\rho_{\mathrm{w}}D_{\mathrm{eq}_i}^3\Delta D_{\mathrm{eq}_i}} \tag{9}$$

for the D14 transformation. (The subscript i is iterated through each size bin.)

Mass-equivalent transformations theoretically ensure that both N_{T} and IWC can be obtained by using the PSD in either form:

$$N_{\mathrm{T}} = \int_0^\infty n_D(D)\,\mathrm{d}D = \int_0^\infty n_{D_{\mathrm{eq}}}(D_{\mathrm{eq}})\,\mathrm{d}D_{\mathrm{eq}}, \tag{10}$$

$$\mathrm{IWC}=\frac{\pi}{6}\int_{0}^{\infty}aD^{b+3}n_D\left(D\right)\mathrm{d}D$$
$$=\frac{\pi}{6}\int_{0}^{\infty}\rho_\mathrm{w}D_\mathrm{eq}^{3}n_{D_\mathrm{eq}}\left(D_\mathrm{eq}\right)\mathrm{d}D_\mathrm{eq},\qquad(11\mathrm{a})$$
$$\mathrm{IWC}=\int_{0}^{\infty}a_\mathrm{m}D^{b_\mathrm{m}}n_D\left(D\right)\mathrm{d}D$$
$$=\frac{\pi}{6}\int_{0}^{\infty}\rho_\mathrm{w}D_\mathrm{eq}^{3}n_{D_\mathrm{eq}}\left(D_\mathrm{eq}\right)\mathrm{d}D_\mathrm{eq}.\qquad(11\mathrm{b})$$

Whether Eq. (11a) or Eq. (11b) is used depends upon whether the D05 or the D14 transformation is being considered. As it turns out, scaling from D space to D_eq space so that Eqs. (10) and (11) are both satisfied is not necessarily possible. Since for the sake of estimating D_m and N_0^* it is more important that IWCs be matched, this was done for the D05 comparison while matching the N_Ts to within a factor of approximately 0.75, plus a bias of $\sim 3.1\,\mathrm{L}^{-1}$.

The following transformation of variables must be used for computing other bulk quantities from transformed PSDs (Bain and Englehardt, 1992):

$$n_D\left(D\right)=n_{D_\mathrm{eq}}\left[D_\mathrm{eq}\left(D\right)\right]\left|\frac{\mathrm{d}D_\mathrm{eq}}{\mathrm{d}D}\right|.\qquad(12)$$

For instance, effective radar reflectivity is computed by integrating over particle maximum dimension intervals, using a set of particle maximum dimension/backscatter power laws that were fit piecewise from T-matrix computations of backscatter cross section to particle maximum dimension (Matrosov, 2007; Matrosov et al., 2012; Hammonds et al., 2014) as follows:

$$Z_\mathrm{e}=\frac{10^8\lambda^4}{|K_w|^2\pi^5}\sum_j\int_{D_j}^{D_{j+1}}a_{zj}D^{b_{zj}}n_{D_\mathrm{eq}}\left[D_\mathrm{eq}\left(D\right)\right]\left|\frac{\mathrm{d}D_\mathrm{eq}}{\mathrm{d}D}\right|\mathrm{d}D.$$

The set of power law coefficients $\left(a_{zj},b_{zj}\right)$ was derived assuming an air–ice dielectric mixing model and that all particles are prolate spheroids with aspect ratios of 0.7 (Korolev and Isaac, 2003; Westbrook et al., 2004a, b; Hogan et al., 2012). Several explicit expressions for computing bulk quantities based on equivalent distributions may be found in Schwartz (2014).

In D05 and D14, data taken with cloud particle and precipitation probes were combined to give PSDs ranging from 25 µm to several millimeters. No precipitation probe data are used here, but how does not including precipitation probe data affect the comparison? This question will be addressed later in this paper.

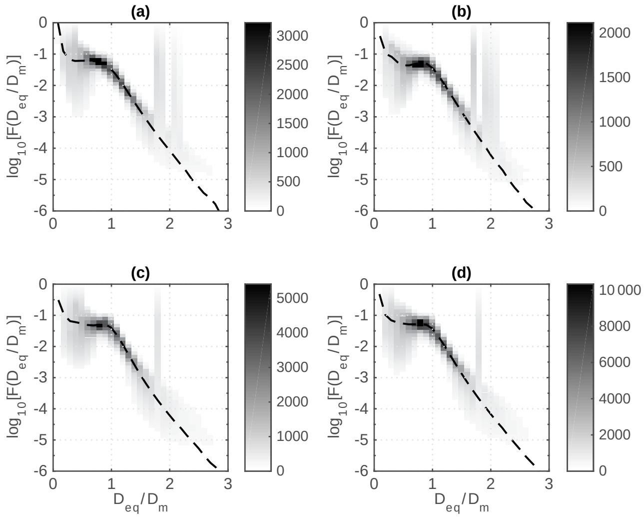

Figure 3. Histograms of normalized PSDs from each flight campaign, overlaid with their mean, normalized PSDs (D05 normalization). The color map is truncated at 75 % of the highest number of samples in a bin so as to increase contrast. **(a)** TC[4], **(b)** MACPEX, **(c)** SPARTICUS, **(d)** all data combined.

Two-dimensional histograms of the normalized PSDs are shown in Fig. 3 for the D05 transformation and in Fig. 5 for the D14 transformation, overlaid with their mean normalized PSDs (cf. Figs. 1 and 2 in D05 and Fig. 3 in D14). For both transformations, the mean normalized PSDs for the three datasets combined are repeated in Figs. 4 and 6 as solid curves (cf. Fig. 3 of D05 and Fig. 6 of D14). These serve as the empirical universal, normalized PSDs $F_{\sim\text{2D-S–D05}}(x)$ and $F_{\sim\text{2D-S–D14}}(x)$, derived using the mass transformations of D05 and D14, respectively. They, along with the quantities derived therefrom, serve to parameterize the more modern 2D-S with shattered-particle removal. The subscripts $\sim$2D-S–D05 and $\sim$2D-S–D14 are used hereinafter to represent bulk quantities derived using $F_{\sim\text{2D-S–D05}}(x)$ and $F_{\sim\text{2D-S–D14}}(x)$.

Three parametric functions for $F(x)$ are given in D05, two of which are repeated here: the gamma-μ function (F_μ) and the modified gamma function ($F_{\alpha,\beta}$; Petty and Huang, 2011).

$$F_\mu\left(x\right)=\frac{\Gamma\left(4\right)}{4}\frac{\left(4+\mu\right)^{4+\mu}}{\Gamma\left(4+\mu\right)}x^\mu\exp\left[-\left(4+\mu\right)x\right]\qquad(13)$$

$$F_{\alpha,\beta}\left(x\right)=\beta\frac{\Gamma\left(4\right)}{4^4}\frac{\Gamma\left(\frac{\alpha+5}{\beta}\right)^{4+\alpha}}{\Gamma\left(\frac{\alpha+4}{\beta}\right)^{5+\alpha}}x^\alpha$$
$$\exp\left[-\left(x\frac{\Gamma\left(\frac{\alpha+5}{\beta}\right)}{\Gamma\left(\frac{\alpha+4}{\beta}\right)}\right)^\beta\right]\qquad(14)$$

Values of μ, α, and β can be chosen to fit these functions to a mean normalized PSD. In D05, the parametric

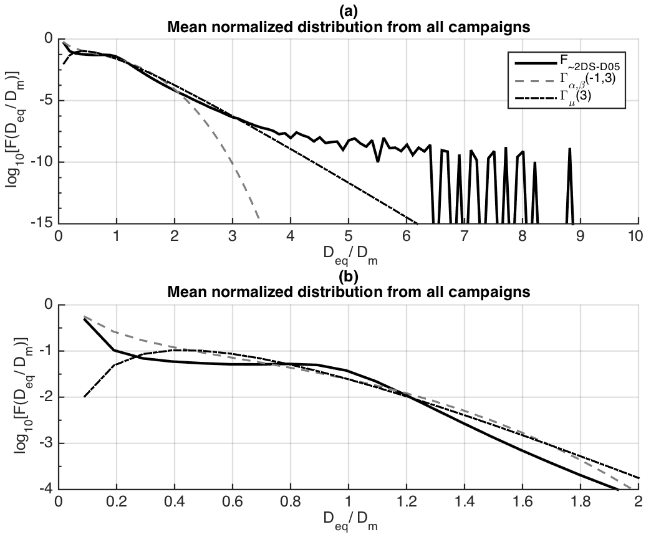

Figure 4. The mean, normalized PSD (D05 normalization) from all three datasets combined, overlaid with two parameterizations from D05: the gamma-μ parameterization (dash-dotted curve) and the modified gamma parameterization (dashed curve). Panel **(b)** is a zoom-in on a portion of panel **(a)**.

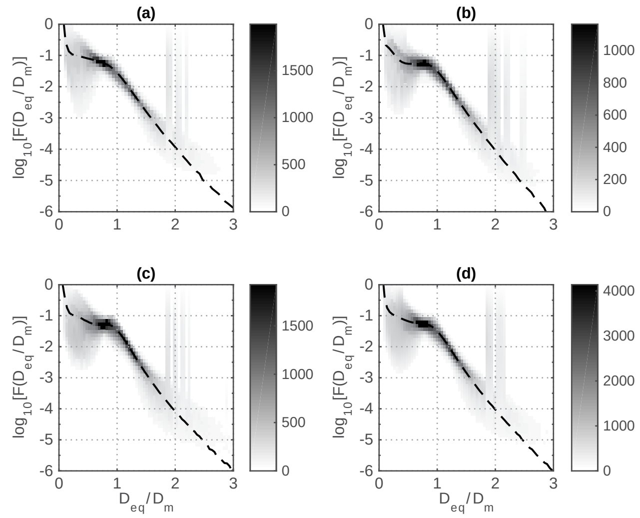

Figure 5. Same as Fig. 3 but using D14 normalization.

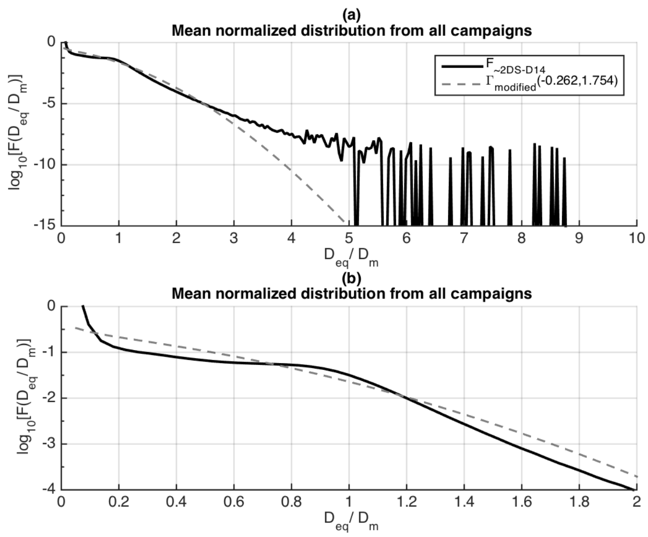

Figure 6. The mean normalized PSD (D14 normalization) from all three datasets combined, overlaid with the parameterizations from D14. Panel **(b)** is a zoom-in on a portion of panel **(a)**.

functions $F_{\alpha,\beta} = F_{(-1,3)}$ (Eq. 14) and $F_\mu = F_3$ (Eq. 13) are given to approximate the universal PSD derived from combined 2DC–2DP datasets; in D14, the parametric function $F_{\alpha,\beta} = F_{(-0.262,1.754)}$ is given to approximate the universal PSD derived from shatter-corrected datasets collected mainly with combined 2DC–2DP probes.

These functions are used to parameterize transformed PSDs measured by the 2DC–2DP, given N_0^* and D_m. We therefore make the assumption that, if we take N_0^* and D_m derived from a 2D-S-measured PSD and then apply them to Eq. (13) or (14), we have effectively simulated the parameterized, transformed PSD that a combined 2DC–2DP would have observed had they been present with the 2D-S. The subscripts $\sim$2DCu and $\sim$2DCs are used hereinafter to represent quantities that simulate 2DC–2DP data (non-shatter-corrected and shatter-corrected, respectively) in this way. Thus, we begin with two versions of $F_{\sim\mathrm{2DCu}}(x)$ – $F_\mu = F_3$ and $F_{\alpha,\beta} = F_{(-1,3)}$ – and one version of $F_{\sim\mathrm{2DCs}}(x)$: $F_{\alpha,\beta} = F_{(-0.262,1.754)}$. Initial observations on comparison of $F_{\sim\mathrm{2D\text{-}S\text{-}D05}}(x)$ and $F_{\sim\mathrm{2D\text{-}S\text{-}D14}}(x)$ with $F_{\sim\mathrm{2DCu}}(x)$ and $F_{\sim\mathrm{2DCs}}(x)$ will now be given.

4.1 Comparison with D05

Some important qualitative observations can be made from examining $F_{\sim\mathrm{2D\text{-}S\text{-}D05}}(x)$ in Fig. 4. First, in contrast to Fig. 3 of D05, the concentrations of particles at the smallest scaled diameters of $F_{\sim\mathrm{2D\text{-}S\text{-}D05}}(x)$ are, on average, about an order of magnitude or more lower than for the mean normalized PSD in D05. From this it is surmised that, while the 2D-S continues to register relatively high numbers of small ice particles, the number has decreased in the newer datasets due to the exclusion of larger numbers of shattered ice crystals.

It can also be seen in Fig. 4 that the shoulder in the normalized PSDs in the vicinity of $x \sim 1.0$ exists in the newer data as it does in the data used in D05. It is worth noting, though, that the shoulder exists in the one tropical dataset used here (TC[4]), whereas it is absent or much less noticeable in the tropical datasets used in D05.

Fortuitously, $F_{\alpha,\beta} = F_{(-1,3)}$ fits the 2D-S data better than it does the older data in D05 at the smallest normalized sizes (cf. Fig. 2 in D05). Neither $F_{\alpha,\beta} = F_{(-1,3)}$ nor $F_\mu = F_3$ correctly catches the shoulder in the newer data, though $F_{\alpha,\beta} =$

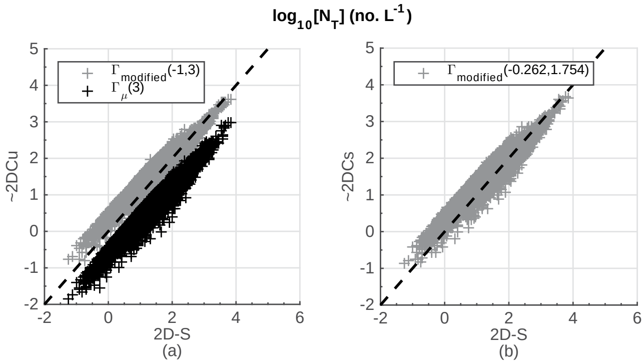

Figure 7. Total number concentration computed using the parameterized universal PSDs from D05 along with true values of N_0^* and D_m (from the 2D-S data) scattered vs. total number concentration computed directly from untransformed 2D-S data.

$F_{(-1,3)}$ was formulated to (better) catch a corresponding shoulder in the older data.

Next, a comparison of PSD quantities computed directly from the 2D-S with corresponding $\sim$2DC-derived quantities (computed using N_0^* and D_m derived directly from the binned 2D-S data and applied to $F_{\alpha,\beta} = F_{(-1,3)}$ and $F_\mu = F_3$) is made. The extinction coefficient, IWC, and 94 GHz radar reflectivity compare well between the 2D-S and both versions of $\sim$2DCu (not shown). As for N_T, it is the least certain computation (see Fig. 7), but $F_\mu = F_3$ is entirely wrong in attempting to reproduce this quantity, so this shape is not used hereinafter, and $F_{\sim 2\mathrm{DCu}}(x) = F_{(-1,3)}(x)$ is the shape used to simulate the uncorrected 2DC–2DP.

Figure 8 shows the mean relative error and the standard deviation of the relative error (cf. Fig. 5 of D05) between 2D-S-derived and corresponding $\sim$2DCu-derived quantities. Effective radius is as defined in D05. Mean relative error for both extinction coefficient and IWC is about -0.1 %. The mean relative error in N_T (N_T computed directly from truncated, binned PSDs is used both here and in Fig. 9) is rather large at ~ 50 %; the mean relative error in Z_e, at ~ 22 %, is larger than that shown in Fig. 5 of D05 (less than 5 % there) but, at about 2 dB, is within the error of most radars. This may well be due to the overestimation of $F(x)$ by $F_{\sim 2\mathrm{DCu}}(x)$ between normalized sizes of about 1.2 and 2 (see Fig. 4b). Both here and in D05, $F_{\sim 2\mathrm{DCu}}(x)$ falls off much more rapidly than $F_{\sim 2\mathrm{D\text{-}S\text{–}D05}}(x)$ above a normalized diameter of 2. However, it is deduced from Figs. 2 and 5 in D05 that this roll-off is not responsible for the large mean relative error in Z shown in Fig. 8.

The mean relative error in effective radius shown in Fig. 8 is approximately -7 %, whereas it is apparently nil in Fig. 5 of D05. Effective radius is defined in D05 as the ratio of the third to the second moments of the spherical-equivalent PSDs and is therefore a weighted mean of the PSD. The negative sign on the relative error indicates that, on average, $F_{\sim 2\mathrm{DCu}}(x)$ is underestimating the effective radius of the PSDs measured by the 2D-S, whereas for the older datasets it hits the effective radius spot on (in the average). Therefore, there is a significant difference between the 2D-S datasets and the older 2DC–2DP datasets in the ratio of large particles to small particles, even when precipitation probe data are not combined with the 2D-S.

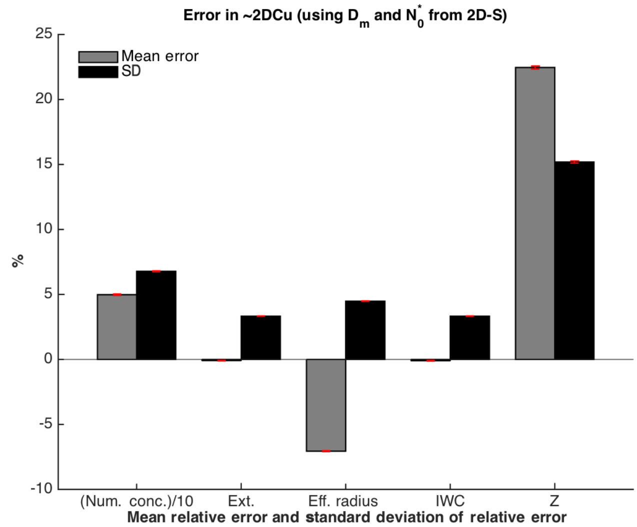

Figure 8. Mean relative error and standard deviation of the relative error between total number concentration (divided by 10), effective radius, IWC, and Z as computed directly from the 2D-S and as computed from the modified-gamma universal PSD shape and the true N_0^* and D_m computed from the 2D-S data. Standard error of the mean and standard deviation are shown with red error bars.

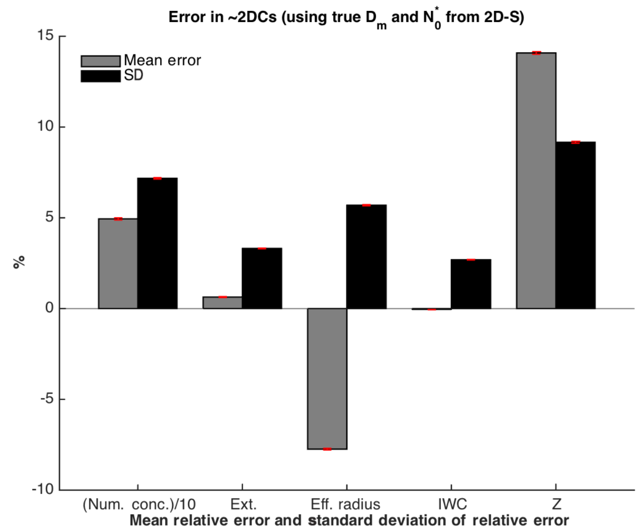

Figure 9. As in Fig. 8 but using the shatter-corrected 2DC parameterization.

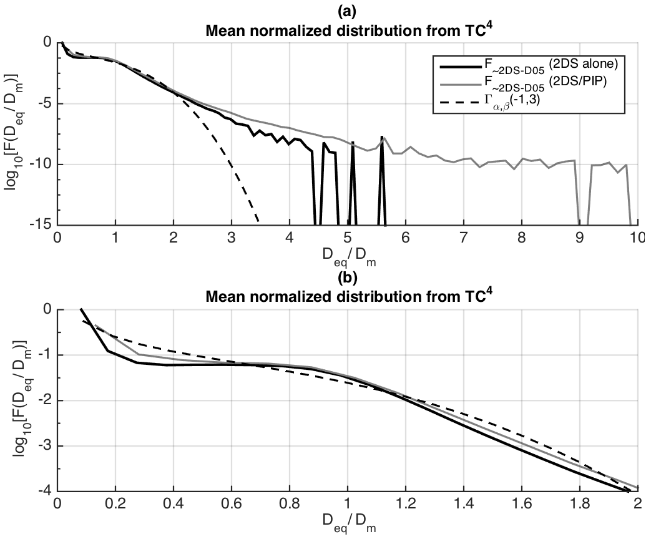

Figure 10. Data from TC[4] alone. The mean normalized PSD from the 2D-S is overlaid with the mean normalized PSD obtained from combining the 2D-S with the PIP and the modified gamma parameterization from D05 (dashed curve). Panel **(b)** is a zoom-in on a portion of panel **(a)**.

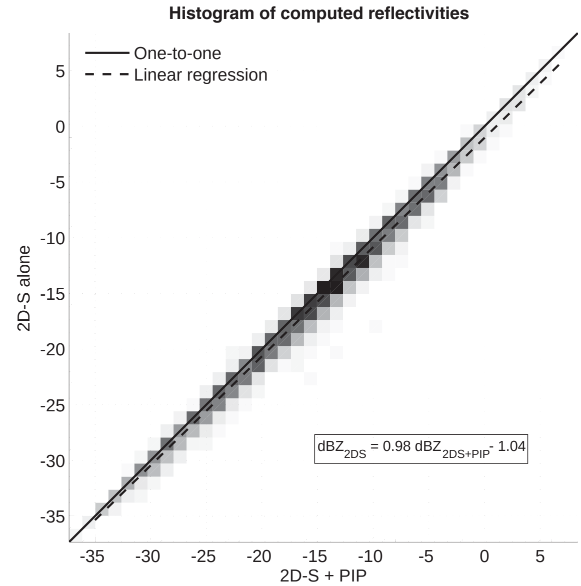

Figure 11. Two-dimensional histogram of 94 GHz effective radar reflectivity computed, using the Hammonds–Matrosov approach, from the 2D-S alone versus that computed from the 2D-S combined with the PIP.

4.2 Comparison with D14

From Fig. 5, concentrations at the smallest scaled diameters of $F_{\sim\text{2D-S–D14}}(x)$ are nominally consistent with those shown in Fig. 6 of D14. In accordance with the surmise made in the comparison with D05 above, it would seem that shattered-particle removal from the 2DC improves comparison between the 2D-S and the 2DC–2DP at the smallest particle sizes.

Here, $F_{\sim\text{2DCs}}(x) = F_{(-0.262,1.754)}(x)$. The shoulder in the normalized PSDs in the vicinity of $x \sim 1.0$ is again found, though the shoulder is not captured by $F_{\sim\text{2DCs}}(x)$ (see Fig. 6). The normalized 2D-S at the smallest normalized sizes is also underestimated by $F_{\sim\text{2DCs}}(x)$. Comparison of N_T computed using $F_{\sim\text{2DCs}}(x)$ with that derived from 2D-S is quite similar to that of $F_{\sim\text{2DCu}}(x)$ (not shown).

As shown in Fig. 9, the mean relative error between N_T and effective radius derived from the 2D-S and from $\sim$2DCs is again about 50 %, while the mean relative error in effective radius remains about −7.5 %. The mean relative error in reflectivity has decreased to about 14 %.

5 Impact of not using precipitation probe data

To more formally investigate the impact of not using a precipitation probe, data from the PIP were combined with data from the 2D-S using the TC[4] dataset. This campaign of the three was chosen due to its tending to occur at warmer temperatures, in a more convective environment, and at lower relative humidities: therefore, if large particles are going to matter, they should matter for TC[4]. Figure 10 shows, similar to Figs. 4 and 6, $F_{\sim\text{2D-S–D05}}(x)$ for the 2D-S alone, $F_{\sim\text{2D-S/PIP–D05}}(x)$ for the 2D-S combined with the PIP, and $F_{\sim\text{2DCu}}(x)$.

In the combined data, $F_{\sim\text{2D-S/PIP–D05}}(x)$ does not dig as low between zero and unity as for the 2D-S alone, but it does show similar numbers of particles at the very smallest normalized sizes, and the shoulder is at the same location. Beginning at about $x = 1.2$, the 2D-S/PIP normalized distribution is higher than the 2D-S-alone normalized distribution, and it continues out to about $x = 10$, whereas the 2D-S-alone distribution ends shy of $x = 5$. In either case, $F_{\sim\text{2DCu}}(x)$ misses what is greater than about $x = 2$. This roll-off, along with the fact that $F_{\sim\text{2D-S/PIP–D05}}(x)$ appears to be more similar to $F_{\sim\text{2D-S–D05}}(x)$ than it does to $F_{\sim\text{2DCu}}(x)$, indicates that a parameterization of $F(x)$ based off the 2D-S alone is comparable to the 2DC/2DP-based $F_{\sim\text{2DCu}}(x)$ parameterization.

In support of this assertion, Fig. 11 shows the penalty in radar reflectivity, computed directly from data using the approach described earlier, incurred by using only the 2D-S instead of the 2D-S-PIP. The penalty is in the neighborhood of 1 dB.

The true (in the sense that they are derived directly from measurements) N_0^* and D_m computed from each of the 2D-S PSDs alone and from the combined PSDs from TC[4] were used, along with $F_{\sim\text{2DCu}}(x)$, to compute N_T, extinction coefficient, IWC, and 94 GHz effective radar reflectivity. This amounts to two different $\sim$2DCu simulations: one including the PIP and one not. The results are shown in Fig. 12.

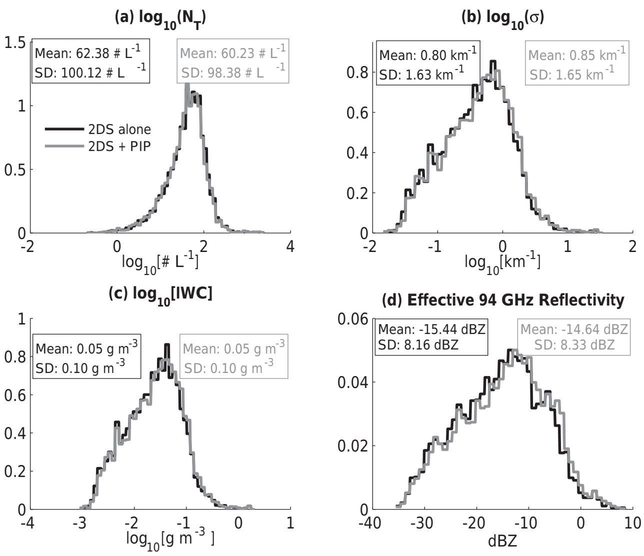

Figure 12. Distributions of quantities computed using the parametric modified gamma distribution along with the true values of N_0^* and D_m computed from the 2D-S alone and from the 2D-S combined with the PIP. **(a)** N_T, **(b)** extinction coefficient, **(c)** IWC, **(d)** 94 GHz effective radar reflectivity.

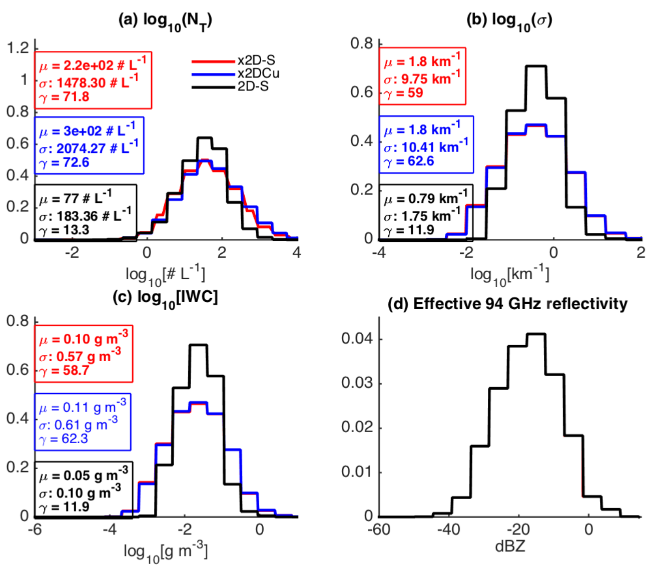

Figure 13. Marginal PDFs of quantities computed directly from 2D-S data, as well as computed using the parameterized 2D-S and the parameterized, uncorrected 2DC. **(a)** Total number concentration, **(b)** shortwave extinction coefficient, **(c)** ice water content, **(d)** radar reflectivity.

The distributions are very similar, with the exception of the reflectivity distributions, whose means are separated by less than 1 dBZ. It is concluded that the cloud filtering technique has resulted in PSDs that are satisfactorily described by the 2D-S alone, at least in the case of this comparison.

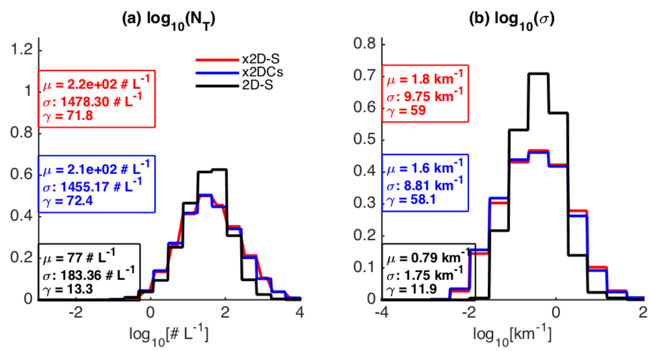

Figure 14. Marginal PDFs of quantities computed directly from 2D-S data, as well as computed using the parameterized 2D-S and the parameterized, corrected 2DC. **(a)** Total number concentration, **(b)** shortwave extinction.

6 Final results and discussion

In D05, complete parameterization of a 2DC–2DP-measured PSD is achieved by using the universal shape $F_{(\alpha,\beta)}(x)$ along with N_0^* parameterized by radar reflectivity and D_m parameterized by temperature. For comparison with the shattered-corrected D14 study, a temperature-based parameterization of "composite"-derived D_m is also computed from the 2D-S data, and "composite"-derived N_0^* is also parameterized by radar reflectivity. A similar parameterization scheme (also based on radar reflectivity and temperature) for the 2D-S (based on Field et al., 2005) is outlined in Schwartz (2014) and is used here to compute a fully parameterized version of 2D-S-measured PSDs so as to make a fair comparison of them with fully parameterized 2DC–2DP-measured PSDs.

Figure 13 shows the results of computing PSD-based quantities using the fully parameterized 2D-S (red, labeled "x2D-S"), using the fully parameterized (uncorrected) 2DC–2DP (blue, labeled "x2DCu"), and directly from the 2D-S data (black). Probability density functions (PDFs) of 94 GHz effective radar reflectivity match because they are forced to by the two instrument parameterizations. Otherwise, biases exist between the two sets of computations based on simulated instruments and computations based on the actual 2D-S (black curve). This bias is due mainly to the temperature parameterization of D_m. The PDFs of extinction coefficient and IWC for the two parameterized instruments match one another quite well (the differences in their medians are not statistically significant). However, for N_T, the x2DCu PDF is shifted to higher concentrations than the PDF for x2D-S. The difference in their medians is statistically significant at the 95 % level according to a Mann–Whitney U test. It is therefore concluded that the older D05 parameterization based on the 2DC–2DP datasets predicts a statistically significantly higher number of total ice crystals than does the parameterized 2D-S (by a factor of about 1.3, or a little over 1 dB) and that, more generally, the 2DC measures a larger ratio of small ice crystals to large ice crystals than does the 2D-S, as shown in the effective radius comparison in Fig. 8.

Figure 14 shows PDFs of N_T and extinction coefficient computed using the fully parameterized 2D-S (red, labeled "x2D-S"), using the fully parameterized (corrected) 2DC–2DP (blue, labeled "x2DCs"), and directly from the 2D-S data (black). The PDFs of extinction match quite well, but their medians are significantly different according to the U test. The medians of N_T are also significantly different, but the mean of the parameterized, corrected 2DC is lower than that of the parameterized 2D-S. A posteriori shatter correction has made 2DC measurements more like 2D-S measurements in the bulk quantity of total particle concentration; however, a statistically significant difference between the 2D-S and the corrected 2DC remains. This result is entirely expected in light of the previous results outlined in the Introduction.

In this paper, an indirect comparison to older 2DC-based datasets by means of parameterizations given in D05 and in D14 has been made. The main discussion points and some sources of uncertainty are now enumerated.

It is determined that the 2D-S cirrus cloud datasets used here are significantly different from historical datasets in numbers of small ice crystals measured. With a posteriori shattered-particle removal applied to older 2DC data, the total numbers of ice crystals measured by the 2D-S and the 2DC become more similar, but NT measured by the 2DC remains statistically different from that measured by the 2D-S.

Given the modest differences found here between bulk cirrus properties derived from PSDs, we conclude that historical datasets continue to be useful. It would seem that for the measurement of bulk cirrus properties – excepting N_T – instrument improvements may have produced only marginal improvements.

It is surmised that – since the efficacy of a posteriori shatter correction on the 2DC is questionable; since the 2D-S is superior in response time, resolution, and sample volume to the 2DC; and since steps were taken to mitigate ice particle shattering on the 2D-S data – the newer datasets are more accurate. Therefore, continuing large-scale field investigations of cirrus clouds using newer particle probes and data processing techniques is recommended. Where possible, investigation of the possibility of statistical comparison and correction of historical cirrus ice particle datasets using newer datasets by flying 2DC probes alongside 2D-S and other more advanced probes is strongly encouraged.

There are some sources of uncertainty.

There exists a large amount of uncertainty in mass–dimensional and density–dimensional relationships for ice crystals, such as those used in D05, in D14, and in this paper. In making a comparison, the best that could be done was to use the same relations in this paper as in D05 and D14. This, of course – depending on which part of the comparison is considered – assumes that the same overall mix of particles habits was encountered between D05 and this study and between D14 and this study.

The data for both D05 and D14 are stated to begin at 25 µm, whereas the 2D-S data used here are truncated to begin at 15 µm. This means that the 2D-S data had the potential of measuring greater numbers of small particles than did the 2DC, and yet the differences in small particles between D05 and the current study were still realized.

Finally, it is important to note that this study does not specifically consider PSD shape. (For a more detailed discussion on cirrus PSD shape and on the efficacy of the gamma distribution, please refer to Schwartz, 2014.) This is a critical component of the answers to the original two questions of Korolov et al. (2013b). Mitchell et al. (2011) demonstrated that, for a given effective diameter and IWC, the optical properties of a PSD are sensitive to its shape. Therefore, PSD bimodality and concentrations of small ice crystals are critical to realistically parameterizing cirrus PSDs, to modeling their radiative properties and sedimentation velocities, and to mathematical forward models designed to infer cirrus PSDs from remote-sensing observations (Lawson et al., 2010; Mitchell et al., 2011; Lawson, 2011). In order to improve knowledge on PSD shape, as well as to develop statistical algorithms for correcting historical PSD datasets so that PSD shapes are corrected along with computations of bulk properties, it will be necessary to make use of instruments that can provide reliable measurements of small ice crystals beneath the size floors of both the 2DC and the 2D-S. Recent studies such as Gerber and DeMott (2014) have provided aspherical correction factors for particle volumes and effective diameters measured by the FSSP. However, the author expects that this problem will ultimately be resolved by the continued technological development of new probes such as the HOLODEC.

Data availability. All SPARTICUS data may be accessed via the Atmospheric Radiation Measurement (ARM) data archive as noted in the references. All MACPEX and TC^4 data may be accessed from the NASA Earth Science Project Office (ESPO) data archive, also noted in the references.

Competing interests. The author declares that he has no conflict of interest.

Acknowledgements. The author gratefully acknowledges the SPARTICUS, MACPEX, and TC^4 science teams for the collection of data used in this study. TC^4 and MACPEX data were obtained from the NASA ESPO archive, which may be accessed online at https://espoarchive.nasa.gov/archive/browse/. The SPARTICUS data were obtained from the Department of Energy (DOE) ARM archive and may be accessed online at http://www.archive.arm.gov/discovery/#v/results/s/fiop::aaf2009Sparticus. In particular, the author acknowledges

Paul Lawson and SPEC Inc. for all 2D-S data collected in the field, Andrew Heymsfield for the PIP data used from TC[4], and Linnea Avallone for CLH data used from MACPEX. Thanks are furthermore given to Gerald G. Mace, Paul Lawson, and Andrew Heymsfield for helpful discussions that led to significant improvements in the manuscript. This work was supported by the US DOE Atmospheric System Research (ASR) – an Office of Science, Office of Biological and Environmental Research (BER) program – under contract DE-AC02-06CH11357 awarded to Argonne National Laboratory. This work was also supported by the National Science Foundation (NSF) grant AGS-1445831. Grateful acknowledgement is also given to the computing resources provided on Blues, a high-performance computing cluster operated by the Laboratory Computing Resource Center (LCRC) at the Argonne National Laboratory.

Edited by: Alexander Kokhanovsky
Reviewed by: Darrel Baumgardner, Jeffrey Reid, and two anonymous referees

References

Bain, L. J. and Englehardt, M.: Introduction to Probability and Mathematical Statistics, 2nd Edn., Duxbury Press, 644 pp., 1992.

Baker, B. A. and Lawson, R. P.: Improvement in determination of ice water content from two-dimensional particle imagery. Part I: Image-to-mass relationships, J. Appl. Meteorol. Clim., 45, 1282–1290, 2006.

Baumgardner, D.: Airborne Measurements for Cloud Microphysics, Res. Aviat. Facility Bull., 24, 1–22, 1989.

Baumgardner, D., Jonsson, H., Dawson, W., O'Connor, D., and Newton, R.: The cloud, aerosol and precipitation spectrometer (CAPS): A new instrument for cloud investigations, Atmos. Res., 59–60, 251–264, https://doi.org/10.1016/S0169-8095(01)00119-3, 2001.

Baumgardner, D., Brenguier, J. L., Bucholtz, A., Coe, H., DeMott, P., Garrett, T. J., Gayet, J. F., Hermann, M., Heymsfield, A., Korolev, A., Krämer, M., Petzold, A., Strapp, W., Pilewskiek, P., Taylor, J., Twohy, C., Wendisch, M., Bachalo, W., and Chuang, P.: Airborne instruments to measure atmospheric aerosol particles, clouds and radiation: A cook's tour of mature and emerging technology, Atmos. Res., 101, 10–29, https://doi.org/10.1016/j.atmosres.2011.06.021, 2011.

Baumgardner, D., Abel, S. J., Axisa, D., Cotton, R., Crosier, J., Field, P., Gurganus, C., Heymsfield, A., Korolev, A., Krämer, M., Lawson, P., McFarquhar, G., Ulanowski, Z., and Um, J.: In situ measurement challenges, Ice Formation and Evolution in Clouds and Precipitation: Measurement and Modeling Challenges, Meteor. Monogr., No. 58, Am. Meteorol. Soc., https://doi.org/10.1175/AMSMONOGRAPHS-D-16-0011.1, 2017.

Brenguier, J.-L., Bachalo, W. D., Chuang, P. Y., Esposito, B. M., Fugal, J., Garrett, T., Gayet, J.-F., Gerber, H., Heymsfield, A., Kokhanovsky, A., Korolev, A., Lawson, R. P., Rogers, D. C., Shaw, R. A., Strapp, W., and Wendisch, M.: In Situ Measurements of Cloud and Precipitation Particles, in: Airborne Measurements for Environmental Research: Methods and Instruments, edited by: Wendisch, M. and Brenguier, J.-L., Wiley-VCH Verlag GmbH & Co. KGaA, Weinheim, Germany, https://doi.org/10.1002/9783527653218.ch5, 2013.

Brown, P. R. A. and Francis, P. N.: Improved Measurements of the Ice Water Content in Cirrus Using a Total Water Probe, J. Atmos. Ocean. Tech., 12, 410–414, 1995.

Cooper, W. A.: Cloud physics investigations by the University of Wyoming in HIPLEX 1977, Department of Atmospheric Science, University of Wyoming, Rep. AS119, 320 pp., 1978.

Davis, S. M., Hallar, A. G., Avallone, L. M., and Engblom, W.: Measurements of Ice Water Content With a Tunable Diode Laser Hygrometer: Calibration Procedure and Inlet Analysis, J. Atmos. Ocean. Tech., 24, 463–475, https://doi.org/10.1175/JTECH1975.1, 2007.

Delanoë, J., Protat, A., Testud, J., Bouniol, D., Heymsfield, A. J., Bansemer, A., Brown, P. R. A., and Forbes, R. M.: Statistical properties of the normalized ice particle size distribution, J. Geophys. Res., 110, https://doi.org/10.1029/2004JD005405, 2005.

Delanoë, J. M. E., Heymsfield, A. J., Protat, A., Bansemer, A., and Hogan, R. J.: Normalized particle size distribution for remote sensing application, J. Geophys. Res., 119, 4204–4227, https://doi.org/10.1002/2013JD020700, 2014.

Demortier, L.: Assessing the Significance of a Deviation in the Tail of a Distribution, Collider Detector at Fermilab note 3419, 1995.

Field, P. R.: Bimodal ice spectra in frontal clouds, Q. J. Roy. Meteor. Soc., 126, 379–392, 2000.

Field, P. R., Wood, R., Brown, P. R. A., Kay, P. H., Hirst, E., Greenaway, R., and Smith, J. A.: Ice Particle Interarrival Times Measured with a Fast FSSP, J. Atmos. Ocean. Tech., 20, 249–261, 2003.

Field, P. R., Hogan, R. J., Brown, P. R. A., Illingworth, A. J., Choularton, T. W., and Cotton, R. J.: Parameterization of ice-particle size distributions for mid-latitude stratiform cloud, Q. J. Roy. Meteor. Soc., 131, 1997–2017, 2005.

Field, P. R., Heymsfield, A. J., and Bansemer, A.: Shattering and particle interarrival times measured by optical array probes in ice clouds, J. Atmos. Ocean. Tech., 23, 1357–1371, 2006.

Fugal, J. P. and Shaw, R. A.: Cloud particle size distributions measured with an airborne digital in-line holographic instrument, Atmos. Meas. Tech., 2, 259–271, https://doi.org/10.5194/amt-2-259-2009, 2009.

Garrett, T. J., Gerber, H., Baumgardner, D. G., Twohy, C. H., and Weinstock, E. M.: Small, highly reflective ice crystals in low-latitude cirrus, Geophys. Res. Lett., 30, 2132, https://doi.org/10.1029/2003GL018153, 2003.

Gayet, J.-F., Auriol, F., Minikin, A., Stroem, J., Seifert, M., Krejci, R., Petzold, A., Febvre, G., and Schumann, U.: Quantitative measurement of the microphysical and optical properties of cirrus clouds with four different in situ probes: 2230, https://doi.org/10.1029/2001GL014342, 2002.

Gayet, J.-F., Ovarlez, J., Shcherbakov, V., Stroem, J., Schumann, U., Minikin, A., Auriol, F., Petzold, A., and Monier, M.: Cirrus cloud microphysical and optical properties at southern and northern midlatitudes during the INCA experiment, J. Geophys. Res., 109, D20206, https://doi.org/10.1029/2004JD004803, 2004.

Gayet, J.-F., Shcherbakov, V., Mannstein, H., Minikin, A., Schumann, U., Stroem, J., Petzgold, A., Ovarlez, J., and Immler, F.: Microphysical and optical properties of midlatitude cirrus clouds observed in the southern hemisphere during INCA, Q. J. Roy. Meteor. Soc., 132, 2719–2748, 2006.

Gerber, H. and DeMott, P. J.: Response of FSSP-100 and PVM-100A to Small Ice Crystals, J. Atmos. Ocean. Tech., 31, 2145–2155, https://doi.org/10.1175/JTECH-D-13-00228.1, 2014.

Gurganus, C. and Lawson, P.: Improvements in Optical Array Probe Characterization: Laboratory and Simulation Results, XVII International Conference on Clouds and Precipitation, Manchester, UK, the International Association of Meteorology and Atmospheric Sciences and the International Commission on Clouds and Precipitation, 2016.

Hammonds, K. D., Mace, G. G., and Matrosov, S. Y.: Characterizing the Radar Backscatter-Cross-Section Sensitivities of Ice-Phase Hydrometeor Size Distributions via a Simple Scaling of the Clausius-Mossotti Factor, J. Appl. Meteorol. Clim., 53, 2761–2774, 2014.

Heymsfield, A. J.: Properties of Tropical and Midlatitude Ice Cloud Particle Ensembles, Part I: Median Mass Diameters and Terminal Velocities, J. Atmos. Sci., 60, 2573–3591, 2003.

Heymsfield, A. J. and McFarquhar, G. M.: High albedos of cirrus in the tropical Pacific warm pool: Microphysical interpretations from CEPEX and from Kwajalein, Marshall Islands, J. Atmos. Sci., 53, 2424–2451, https://doi.org/10.1175/1520-0469(1996)053<2424:HAOCIT>2.0.CO;2, 1996.

Heymsfield, A. J., Bansemer, A., Field, P. R., Durden, S. L., Stith, J. L., Dye, J. E., Hall, W., and Grainger, C. A.: Observations and Parameterizations of Particle Size Distributions in Deep Tropical Cirrus and Stratiform Precipitating Clouds: Results from In Situ Observations in TRMM Field Campaigns, J. Atmos. Sci., 59, 3457–3491, 2002.

Heymsfield, A. J., Bansemer, A., Heymsfield, G., and Fierro, A. O.: Microphysics of Maritime Tropical Convective Uprafts at Temperatures from −20° to −60 °C, J. Atmos. Sci., 66, 3530–3562, 2009.

Heymsfield, A. J., Schmitt, C., Bansemer, A., and Twohy, C. H.: Improved representation of ice particle masses based on observations in natural clouds, J. Atmos. Sci., 67, 3303–3318, https://doi.org/10.1175/2010JAS3507.1, 2010.

Heymsfield, A. J., Krämer, M., Luebke, A., Brown, P., Cziczo, D. J., Franklin, C., Lawson, P., Lohmann, U., McFarquhar, G., Ulanowski, Z., and Van Tricht, K.: Cirrus Clouds, Meteorol. Monogr., 58, 2.1–2.26, https://doi.org/10.1175/AMSMONOGRAPHS-D-16-0010.1, 2017.

Hobbs, P. V. and Rangno, A. L.: Ice particle concentrations in clouds, J. Atmos. Sci., 42, 2523–2549, 1985.

Hogan, R. J., Tian, L., Brown, P. R. A., Westbrook, C. D., Heymsfield, A. J., and Eastment, J. D.: Radar Scattering from Ice Aggregates Using the Horizontally Aligned Oblate Spheroid Approximation, J. Appl. Meteorol. Clim., 51, 655–671, 2012.

Jackson, R. C. and McFarquhar, G. M.: An Assessment of the Impact of Antishattering Tips and Artifact Removal Techniques on Bulk Cloud Ice Microphysical and Optical Properties Measured by the 2D Cloud Probe, J. Atmos. Ocean. Tech., 30, 2131–2144, 2014.

Jackson, R. C., McFarquhar, G. M., Stith, J., Beals, M., Shaw, R. A., Jensen, J., Fugal, J., and Korolev, A.: An Assessment of the Impact of Antishattering Tips and Artifact Removal Techniques on Cloud Ice Size Distributions Measured by the 2D Cloud Probe, J. Atmos. Ocean. Tech., 31, 2576–2590, 2014.

Jensen, E. J., Lawson, P., Baker, B., Pilson, B., Mo, Q., Heymsfield, A. J., Bansemer, A., Bui, T. P., McGill, M., Hlavka, D., Heymsfield, G., Platnick, S., Arnold, G. T., and Tanelli, S.: On the importance of small ice crystals in tropical anvil cirrus, Atmos. Chem. Phys., 9, 5519–5537, https://doi.org/10.5194/acp-9-5519-2009, 2009.

Khain, A., Pinsky, M., Elperin, T., Kleeorin, N., Rogachevskii, I., and Kostinski, A.: Critical comments to results of investigations of drop collisions in turbulent clouds, Atmos. Res., 86, 1–20, 2007.

Knollenburg, R.: Three new instruments for cloud physics measurements: The 2-D spectrometer probe, the forward scattering spectrometer probe, and the active scattering aerosol spectrometer, Preprints, Int. Conf. on Cloud Physics, Boulder, CO, Am. Meteor. Soc., 554–561, 1976.

Knollenburg, R.: Techniques for probing cloud microstructure, Clouds, Their Formation, Optical Properties and Effects, edited by: Hobbs, P. V. and Deepak, A., Academic Press, 15–91, 1981.

Korolev, A. and Field, P. R.: Assessment of the performance of the inter-arrival time algorithm to identify ice shattering artifacts in cloud particle probe measurements, Atmos. Meas. Tech., 8, 761–777, https://doi.org/10.5194/amt-8-761-2015, 2015.

Korolev, A. V. and Isaac, G.: Roundness and Aspect Ratio of Particles in Ice Clouds, J. Atmos. Sci., 60, 1795–1808, 2003.

Korolev, A. V., Emery, E. F., Strapp, J. W., Cober, S. G., Isaac, G. A., Wasey, M., and Marcotte, D.: Small Ice Particles in Tropospheric Clouds: Fact or Artifact?, B. Am. Meteor. Soc., 92, 967–973, 2011.

Korolev, A. V., Emery, E., and Creelman, K.: Modification and Tests of Particle Probe Tips to Mitigate Effects of Ice Shattering, J. Atmos. Ocean. Tech., 30, 690–708, 2013a.

Korolev, A. V., Emerty, E. F., Strapp, J. W., Cober, S. G., and Isaac, G. A.: Quantification of the effects of Shattering on Airborne Ice Particle Measurements, J. Atmos. Ocean. Tech., 30, 2527–2553, 2013b.

Kostinski, A. B. and Shaw, R. A.: Scale-dependent droplet clustering in turbulent clouds, J. Fluid. Mech., 434, 389–398, 2001.

Lance, S., Brock, C. A., Rogers, D., and Gordon, J. A.: Water droplet calibration of the Cloud Droplet Probe (CDP) and in-flight performance in liquid, ice and mixed-phase clouds during ARCPAC, Atmos. Meas. Tech., 3, 1683–1706, https://doi.org/10.5194/amt-3-1683-2010, 2010.

Lawson, R. P.: Effects of ice particles shattering on the 2D-S probe, Atmos. Meas. Tech., 4, 1361–1381, https://doi.org/10.5194/amt-4-1361-2011, 2011.

Lawson, R. P., Stewart, R. E., and Angus, L. J.: Observations and numerical simulations of the origin and development of very large snowflakes, J. Atmos. Sci., 55, 3209–3229, https://doi.org/10.1175/1520-0469(1998)055<3209:OANSOT>2.0.CO;2, 1998.

Lawson, R. P., Baker, B., Pilson, B., and Mo, Q.: In Situ Observations of the Microphysical Properties of Wave, Cirrus, and Anvil Clouds, Part II: Cirrus Clouds, J. Atmos. Sci., 63, 3186–3203, 2006.

Lawson, R. P., Jensen, E., Mitchell, D. L., Baker, B., Mo, Q., and Pilson, B.: Microphysical and radiative properties of tropical clouds investigated in TC4 and NAMMA, J. Geophys. Res., 115, D00J08, https://doi.org/10.1029/2009JD013017, 2010.

Locatelli, J. D. and Hobbs, P. V.: Fall speed and masses of solid precipitation particles, J. Geophys. Res., 79, 2185–2197, 1974.

MACPEX Science Team: MACPEx, NASA Earth Science Project Office Data Archive, available at: https://espoarchive.nasa.gov/archive/browse/macpex (last access: 31 March 2013), 2011.

Matrosov, S. Y.: Modeling Backscatter Properties of Snowfall at Millimeter Wavelengths, J. Atmos. Sci., 64, 1727–1736, 2007.

Matrosov, S. Y., Mace, G. G., Marchand, R., Shupe, M. D., Hallar, A. G., and McCubbin, I. B.: Observations of Ice Crystal Habits with a Scanning Polarimetric W-Band Radar at Slant Linear Depolarization Ratio Mode, J. Atmos. Ocean. Tech., 29, 989–1008, 2012.

McFarquhar, G. M., Um, J., Freer, M., Baumgardner, D., Kok, G. L., and Mace, G.: Importance of small ice crystals to cirrus properties: Observations from the Tropical Warm Pool International Cloud Experiment (TWP-ICE), Geophys. Res. Lett., 34, L13803, https://doi.org/10.1029/2007GL029865, 2007.

Meakin, P.: Aggregation kinetics, Phys. Scripta, 46, 295–331, 1992.

Mitchell, D. L., Lawson, R. P., and Baker, B.: Understanding effective diameter and its application to terrestrial radiation in ice clouds, Atmos. Chem. Phys., 11, 3417–3429, https://doi.org/10.5194/acp-11-3417-2011, 2011.

Moon, T. K.: The Expectation-Maximization Algorithm, IEEE Signal Proc. Mag., 13, 47–60, 1996.

Petty, G. W. and Huang, W.: The Modified Gamma Size Distribution Applied to Inhomogenous and Nonspherical Particles: Key Relationships and Conversions, J. Atmos. Sci., 68, 1460–1473, 2011.

Pinsky, M. and Khain, A.: Fine structure of cloud droplet concentration as seen from the Fast-FSSP measurements, Part II: Results of in situ observations, J. Appl. Meteorol. Clim., 42, 65–73, 2003.

Schwartz, M. C.: Analysis of Cirrus Particle Size Distributions from Three In Situ Flight Campaigns: Applications to Cirrus Microphysics and Parameterization, Remote Sensing, and Radar Forward Model Simulators, PhD dissertation, Dept. of Atmospheric Sciences, the University of Utah, 229 pp., 2014.

SPARTICUS Science Team: SPartICus, Atmospheric Radiation Measurement Data Archive, PI/Campaign Data, available at: http://www.archive.arm.gov/discovery/#v/results/s/fiop::aaf2009Sparticus (last access: 26 March 2013), 2010.

TC^4 Science Team: TC4 DC-8 files, NASA Earth Science Project Office Data Archive, available at: https://espoarchive.nasa.gov/archive/browse/tc4/DC8 (last access: 29 March 2012), 2007.

Tinel, C., Testud, J., Pelon, J., Hogan, R. J., Protat, A., Delanoe, J., and Bouniol, D.: The retrieval of ice-cloud properties from cloud radar and lidar synergy, J. Appl. Meteor., 44, 860–875, 2005.

Ulanowski, Z., Kaye, P. H., Hirst, E., Greenaway, R. S., Cotton, R. J., Hesse, E., and Collier, C. T.: Incidence of rough and irregular atmospheric ice particles from Small Ice Detector 3 measurements, Atmos. Chem. Phys., 14, 1649–1662, https://doi.org/10.5194/acp-14-1649-2014, 2014.

Vidaurre, G. and Hallett, J.: Particle Impact and Breakup in Aircraft Measurement, J. Atmos. Ocean. Tech., 26, 972–983, 2009.

Westbrook, C. D., Ball, R. C., Field, P. R., and Heymsfield, A. J.: Universality in snowflake aggregation, Geophys. Res. Lett., 31, L15104, https://doi.org/10.1029/2004GL020363, 2004a.

Westbrook, C. D., Ball, R. C., Field, P. R., and Heymsfield, A. J.: Theory of growth by differential sedimentation, with application to snowflake formation, Phys. Rev. E, 70, 021403–021409, https://doi.org/10.1103/PhysRevE.70.021403, 2004b.

Wilks, D. S.: Statistical Methods in the Atmospheric Sciences, 2nd Edn., Academic Press, 627 pp., 2006.

Zhao, Y., Mace, G. G., and Comstock, J. M.: The occurrence of particle size distribution bimodality in midlatitude cirrus as inferred from ground-based remote sensing data, J. Atmos. Sci., 68, 1162–1176, 2011.